# General Route to Nanocrystalline Oxides by Hydrodynamic Cavitation

Joseph E. Sunstrom IV, William R. Moser,* and Barbara Marshik-Guerts

*Department of Chemical Engineering, Worcester Polytechnic Institute, Worcester, Massachusetts 01609*

*Received December 20, 1995. Revised Manuscript Received May 3, 1996*[⊗]

We have developed the WPI cavitational materials process for the production of phase-pure, nanostructured materials. Hydrodynamic cavitation is generated mechanically using a high-pressure fluid system. The method begins with a precipitant stream that experiences a large pressure drop (21 000 psi ambient) across a patented geometry interaction chamber. Due to the large pressure drop, bubbles are formed and collapse, causing localized heating of the solvent. In addition, the precipitate undergoes a high degree of mechanical shear in the interaction chamber. This paper deals with the application of this novel technique to the synthesis of several nanostructured oxides. The nanophase oxides are characterized using transmission electron microscopy, X-ray diffraction, thermal gravimetric analysis, differential scanning calorimetry, and Fourier transform infrared spectroscopy. Select area diffraction patterns of the dried (110 °C) oxide samples in this study show distinct rings indicating nanosized particles. This is corroborated by peak breadth measurements in the X-ray diffraction patterns of the calcined samples. A comparison is made between cavitation syntheses and classical coprecipitation.

## Introduction

Recently, there has been significant interest in the study of nanostructured materials. The interest in nanostructured materials originates from the fact that small nanoparticles have a higher surface/bulk atom ratio.[1] The free energy of surface ions is higher than those in the bulk, which means that nanoparticles will have increased surface energy. As discussed previously, the increased fraction of surface atoms will affect the grain boundary structure and the interaction of grains with one another in polycrystalline samples.[1−7] This should manifest itself in significant effect upon macroscopic properties such as catalytic activity and electronic properties. Small particle size is an added benefit in heterogeneous catalysis since it affords larger surface area and higher concentration of surface metal sites for modification with other ions. Also, there is an inherent higher ratio of low coordination edge to basal plane sites. Most of the current interest in nanostructured materials is due to advances in synthesis and isolation techniques. There have been extensive reviews dealing with synthetic techniques of nanocrystals.[8−12]

We have been exploring the use of hydrodynamic cavitation to synthesize a number of useful nanostructured materials. The causes and effects of the cavitation phenomena have previously been detailed.[13] Suslick and co-workers have demonstrated the utility of sound-wave-generated cavitation in a number of processes, including the synthesis of new materials.[14−20] In this study, the recently developed WPI cavitational materials process generates hydrodynamic cavitation mechanically using a Microfluidizer. The Microfluidizer is a fluid processing system that utilizes a patented fixed geometry mixing chamber with an electrohydraulic pumping system. This material processing method begins with the coprecipitation of the metal oxide component gel immediately before the inlet to port B in Figure 1. The slurry is then drawn into the device where it experiences a large rise in pressure from ambient atmospheric pressure to 21 000 psi. Upon entering the cavitation chamber, the process stream is diverted into two equal streams that are redirected in such a way as to impinge on one another at 180° in a low-volume chamber while traveling at high velocity. The impinging streams experience an exceptionally high mechanical shear. The process stream also experiences a pressure drop from 21 000 psi to ambient pressure upon exiting the chamber. This rapid pressure decrease

* To whom correspondence should be addressed.

[⊗] Abstract published in *Advance ACS Abstracts,* July 15, 1996.

(1) Siegel, R. W. *Annu. Rev. Mater. Sci.* **1991**, *21*, 559.
(2) Gleiter, H. *Prog. Mater. Sci.* **1990**, *33*, 223.
(3) Siegel, R. W. *MRS Bull.* **1990**, *15(10)*, 60.
(4) Siegel, R. W. *Materials Science and Technology—A Comprehensive Treatment*; Cahn, R. W., Ed.; VCH: Weinheim, 1991; Vol. 15, p 583.
(5) Birringer, R.; Gleiter, H. *Encyclopedia of Materials Science and Engineering*; Cahn, R. W., Ed.; Pergamom Press; Oxford, 1988; Suppl. Vol. 1, p 339.
(6) Siegel, R. W.; Thomas, G. J. *Ultramicroscopy* **1992**, *40*, 376.
(7) Bush, M. B. *Mater. Sci. Eng.* **1993**, *A161*, 127.
(8) Siegel, R. W. *Mater. Sci. Eng.* **1993**, *A168*, 189.
(9) Siegel, R. W. *Mechanical Properties and Deformation Behavior of Materials Having Ultra-Fine Microstructures*; Nastasi, M., Parkin, D. M., Gleiter, H., Eds.; Kluwer: Dordrecht, 1993; p 509.
(10) Ozin, G. A. *Adv. Mater.* **1992**, *4*, 612.
(11) Eastman, J.; Siegel, R. W. *Res. Dev.* **1989**, *Jan*, 56.
(12) Gleiter, H. *Proc. Mater. Sci.* **1989**, *33*, 223.
(13) Young, F. R. *Cavitation*; McGraw Hill: New York, 1989.
(14) Suslick, K. S. *Mater. Res. Soc. Bull.* **1995**, *20*, 29.
(15) Suslick, K. S.; Fang, M.; Hyeon, T.; Cichowlas, A. A. *Mater. Res. Soc. Symp. Proc.* **1994**, *351*, 443.
(16) Grinstaff, M. W.; Salamon, M. B.; Suslick, K. S. *Phys. Rev. B* **1993**, *48*, 2269.
(17) Grinstaff, M. W.; Cichowlas, A. A.; Choe, S. B.; Suslick, K. S. *Ultrasonics* **1992**, *30*, 168.
(18) Suslick, K. S.; Coe, S. B.; Cichowlas, A. A.; Grinstaff, M. W. *Nature* **1991**, *353*, 414.
(19) Suslick, K. S. *Science* **1990**, *247*, 1439.
(20) Suslick, K. S. In Suslick, K. S., Ed. *Ultrasound: Its Chemical, Physical, and Biological Effects*; VCH Press: New York, 1988; p 123.

S0897-4756(95)00609-0 CCC: $12.00 

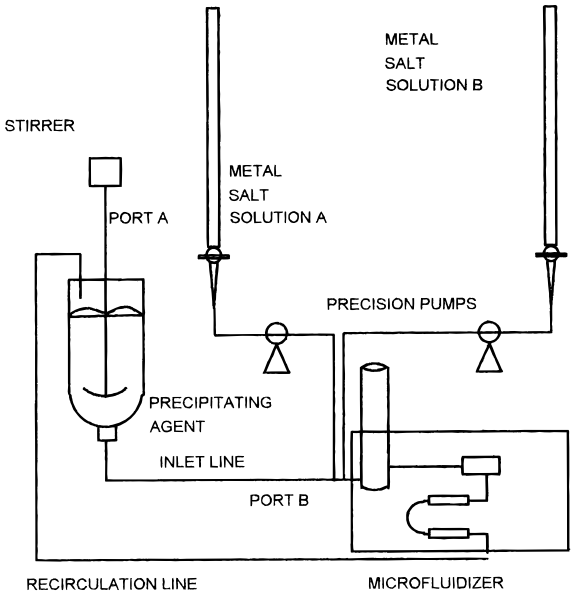


**Figure 1.** Schematic of cavitation synthesis (reproduced with permission of *Journal of Materials Research*).

at high velocity causes the solvent to boil and a hydrodynamic wake of bubbles to form. This phenomenon is explained by the Bernoulli effect. The formation and subsequent implosion of the bubbles cause local cavitational heating of the precipitant stream. This cavitational heating coupled with the high shear experienced by the process stream are essential components in the production of high-quality nanophase materials. In addition, we have shown previously that it is possible to form phase-pure complex oxides due to the high degree of mixing which occurs in this synthetic method.[21]

Simple oxides are used in a broad range of applications such as catalytic, electronic, magnetic, and optical materials. Nanophase synthesis of simple oxides has not been explored in great detail. This paper details the synthesis and characterization of some nanostructured simple oxides. It is part of an ongoing study in our laboratory of hydrodynamic cavitation as a viable synthetic method for many types of nanostructured materials.

## Experimental Section

**Synthesis.** Metal nitrate salts (Alfa or Aldrich) were used directly as received and were purchased as a minimum of reagent-grade purity. Titanium tetrabutoxide was purchased from Aldrich. All cavitation experiments were carried out using a Model M-110EH microfluidizer manufactured by Microfluidics International Inc. of Newton, MA.

With exception of titania, all syntheses were completed with 100 mL metal nitrate solutions (0.25−0.5 M) as precursors (see Table 1 for gram amounts). The precipitating agent was either 1 M aqueous ammonium hydroxide (Zr, Co, Cr, Ce, Y) or 1 M KOH in ethanol (Ni). The precursor for the titania synthesis was titanium tetrabutoxide/isopropanol solution and the precipitating agent was 5% v/v water/ethanol.

All metal nitrate solutions were fed by means of a peristaltic pump at 3.3 mL/min into a reservoir containing 500 mL of precipitating agent. The precipitation reaction occurs at the inlet to the high-pressure pump, leading to the cavitation chamber to help minimize crystal growth. All reactions were carried out at a reaction pressure of 21 000 psi. The process stream was allowed to recirculate into the reservoir of the metal salt. The total reaction time was 30 min, and no additional recirculation of the precipitate was performed.

**Table 1. Gram Amounts of Metal Nitrate Precursors**

| precursor | mass (g) |
|---|---|
| $ZrO(NO_3)_2 \cdot xH_2O$ | 4.989 |
| $Ni(NO_3)_2 \cdot 6H_2O$ | 19.523 |
| $Ce(NO_3)_3 \cdot 6H_2O$ | 10.715 |
| $Co(NO_3)_2 \cdot 6H_2O$ | 14.560 |
| $Fe(NO_3)_3 \cdot 9H_2O$ | 10.101 |
| $Y(NO_3)_3 \cdot 6H_2O$ | 11.502 |
| $Cr(NO_3)_3 \cdot 9H_2O$ | 12.121 |

The resulting precipitate was then collected and filtered using a pressure filter (60 psi) with a 0.2 $\mu$m membrane (Gelman). The precipitates were then washed with isopropanol and dried at 110 °C for 12 h.

**X-ray Diffraction.** X-ray diffraction data were collected on a Phillips XRG-3000 diffractometer utilizing Ni-filtered Cu K$\alpha$ ($\lambda = 1.54$ Å) radiation. Samples were placed in aluminum sample holders and scanned from 10 to 85° 2$\theta$ in 0.2° steps. The count rate was 4 s/step.

**Transmission Electron Microscopy.** Transmission electron micrographs and selected area diffraction patterns were obtained on a JEOL 100C transmission electron microscope. The camera constant for the selected area diffraction (SAD) ring patterns was obtained by measuring the ring pattern for a thin gold foil sputtered onto a grid. Solid samples were dried at 110−200 °C for 12 h and then suspended in dry 2-propanol and sonicated 1−2 min. The suspensions were placed, without thinning, on holey carbon grids. The samples were immediately examined due to rapid moisture uptake. The samples were focused, and then the grid was moved to minimize heating by the electron beam.

**Thermal Analysis.** Thermal gravimetric analyses (TGA) were performed using a DuPont Model 951 thermogravimetric analyzer. Approximately 50 mg of sample was placed in platinum boats hung from a quartz microbalance. The experiments were performed under flowing air or $N_2$ (50 $cm^3$/min). Differential scanning calorimetry was performed using a DuPont cell base with high-pressure DSC cell. The samples were placed into aluminum sample pans and placed into 100 psi air at room temperature. The samples for both TGA and DSC analyses were allowed to isotherm at 100 °C for 3 h to allow removal of ambient moisture. The samples were then allowed to ramp at 5 °C/min to 550 °C.

**Fourier Transform Infrared Spectroscopy.** Infrared analyses were performed on select samples using a Perkin-Elmer FTIR. The samples were prepared as 25 mg of 5% w/w oxide/KBr pellets. The spectra are an average of 16 scans from 400 to 4000 $cm^{-1}$.

## Results and Discussion

This study describes the synthesis and characterization of several simple metal oxides prepared as nanostructured materials by the WPI cavitational materials synthesis process.[22,23] A wide variety of simple metal oxides was prepared using this method. The properties described below for the $TiO_2$, $ZrO_2$, NiO, and $CeO_2$ were typical of the behavior of the other materials in this study.

**$TiO_2$.** Nanophase titania was isolated as a fine white powder upon drying at 110 °C for 12 h. The SAD pattern of the cavitation synthesis dried titania has been shown previously.[21] Figure 2a,b show the titania sample after drying at 110 °C and calcining at 500 °C, respectively. The rings can be indexed to the α-anatase

(21) Moser, W. R.; Marshik, B. J.; Kingsley, J.; Lemberger, M.; Willette, R.; Chan, A.; Sunstrom IV, J. E.; Boye, A. *J. Mater. Res.* **1995**, *10*, 2322.

(22) Moser, W. R. U.S. Patent 5,417,956, Assigned to Worcester Polytechnic Institute, 1995.

(23) Moser, W. R. U.S. Patent, 5,466,646, Assigned to Worcester Polytechnic Institute, 1995.

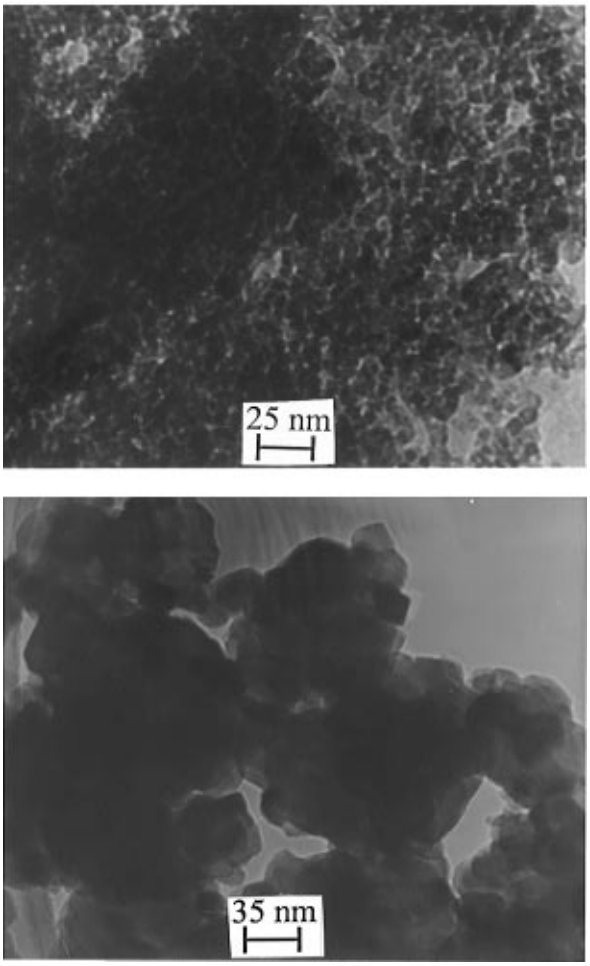


**Figure 2.** (a, top) TEM micrograph of dried (110 °C) $TiO_2$. (b, bottom) TEM micrograph of calcined (500 °C) $TiO_2$.

**Table 2. Comparison of SAD *d* Spacings for $TiO_2$ with JCPDS File for $TiO_2$ (Anatase)**

| $d_{obsd}$ | $d_{JCPDS}$ | $d_{obsd}$ | $d_{JCPDS}$ |
|---|---|---|---|
| 3.52 | 3.52 | 1.49 | 1.493 |
| | 2.431 | | 1.4808 |
| 2.38 | 2.378 | 1.34 | 1.3378 |
| | 2.332 | 1.25 | 1.2509 |
| 1.89 | 1.892 | 0.99 | 0.9967 |
| 1.67 | 1.6665 | 0.95 | 0.945 |

structure type. Table 2 shows a comparison of observed *d* spacings with the JCPDS file for α-anatase. The anatase structure type is consistent with previous syntheses of nanostructured titania.[24]

The TEM micrograph (see Figure 2a) of the dried titania sample shows the primary particle sizes to be on the order of 1−3 nm. Figure 3 shows the X-ray patterns of the sample at several temperatures. There is no appearance of diffraction peaks until 300 °C. The diffraction pattern at 300−500 °C can be indexed to the anatase structure type. The Debye−Scherrer equation yields a particle size of 3.4 nm.

Figure 4 shows the TGA/DSC data for the titania sample. The DSC trace consists of two exothermic peaks at approximately 265 °C (peak A) and 440 °C (peak B). Peak A (Figure 3) is due to the water loss and subsequent crystallization of remaining amorphous titania. The TGA shows that the weight loss is equal

(24) Kormann, C.; Bahnemann, D. W.; Hoffman, M. R. *J. Phys. Chem.* **1988**, *92*, 5196.

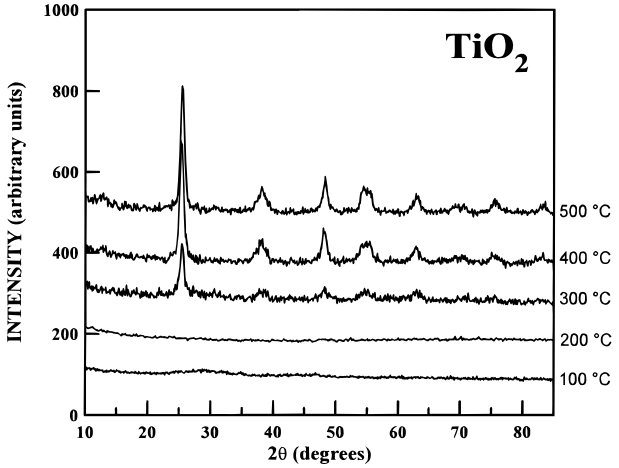


**Figure 3.** X-ray diffraction traces for $TiO_2$ heated at 100−500 °C (from bottom to top).

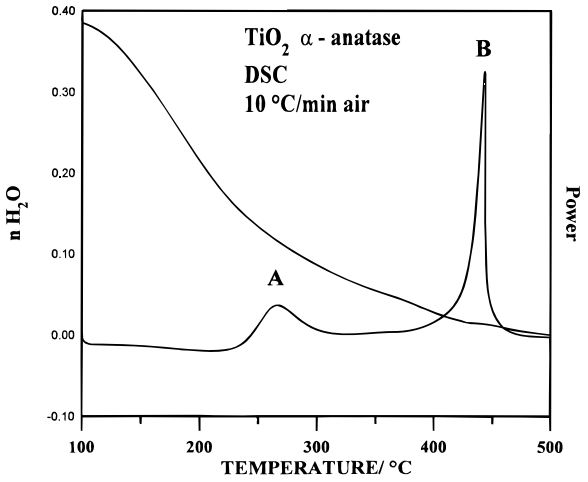


**Figure 4.** Thermal gravimetric analysis and differential scanning calorimetry traces from 100 to 500 °C in air for nanophase titania.

to 0.38 $H_2O$/formula unit. This means a significant amount of the product is the oxide and the balance is either hydroxide or surface-bound water. The water loss for the $Ti(OH)_2 \rightarrow TiO_2$ transition would be 2 $H_2O$/formula unit. Peak B (Figure 3) is consistent with rapid crystal grain growth. First, there is not significant water loss at this point in the TGA trace, meaning that this exotherm is a physical change as opposed to a chemical change. The rapid grain growth is clearly due to the nature of the experiment (i.e., furnace ramp rate). There is a kinetic effect introduced by the high ramp rate and the compound achieves the activation energy needed for rapid crystallization at an elevated temperature (440 °C). This is in contrast to the X-ray diffraction traces for $TiO_2$ that begin to show crystal growth at 300 °C. For the diffraction experiments, the samples were allowed to sit at the calcination temperatures for several hours. This shows that controlled calcination along with synthetic technique is an important component in achieved desired particle size. Peak B (Figure 3) is consistent with grain growth as clearly evidenced in the TEM of the calcined sample (Figure 2b) which shows significant grain growth.

**$ZrO_2$.** Zirconia gels were prepared by two methods. In addition to the cavitation synthesis, a classical coprecipitation synthesis was completed. The metal salt solution and precipitating agent was prepared and split

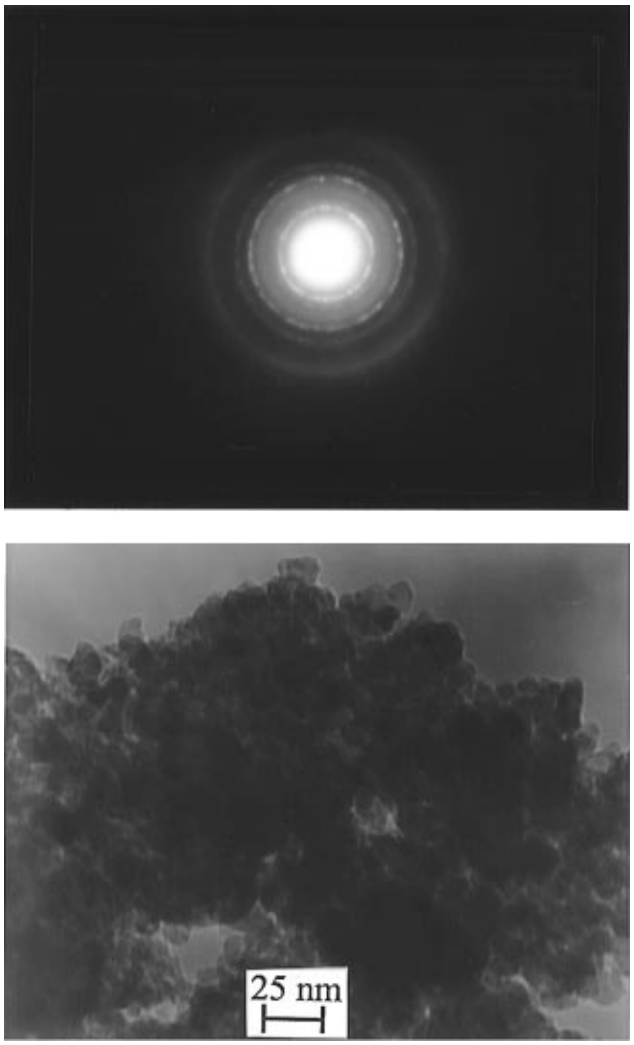


**Figure 5.** (a, top) Select area diffraction pattern for dried (110 °C) $ZrO_2$. (b, bottom) TEM micrograph for dried (110 °C) $ZrO_2$.

**Table 3. Comparison of SAD *d* Spacings for $ZrO_2$ with JCPDS File for $ZrO_2$ (Cubic)**

| $d_{obsd}$ | $d_{JCPDS}$ | $d_{obsd}$ | $d_{JCPDS}$ |
|---|---|---|---|
| 2.94 | 2.93 | 1.27 | 1.270 |
| 2.54 | 2.55 | 1.14 | 1.135 |
| 1.80 | 1.801 | 1.04 | 1.038 |
| 1.54 | 1.535 | | |

to ensure identical concentrations in both syntheses. The metal salt addition time, stirring time, and pH were kept constant in both the classical and cavitation syntheses.

The solids isolated upon drying at 110 °C for 12 h were green (cavitation) and yellow (classical). Transmission electron microscopy of the classical sample showed aggregate sizes approaching 1 $\mu$m. It was not possible to get an electron diffraction of the classical sample due to thickness of the aggregates. Aggregate sizes for the cavitation sample were 50−100 nm in size. Figure 5a shows a SAD pattern of the cavitation sample that can be indexed as cubic zirconia. A halo is also present indicating presence of amorphous product in the sample. Table 3 is a comparison of the indexed diffraction rings with the JCPDS entry for cubic zirconia. Figure 5b shows a TEM micrograph of the zirconia sample that shows the primary particle sizes to be 5−10 nm. The particle size yielded by the Debye−Scherrer equation is 8.2 nm. An X-ray diffraction pattern for

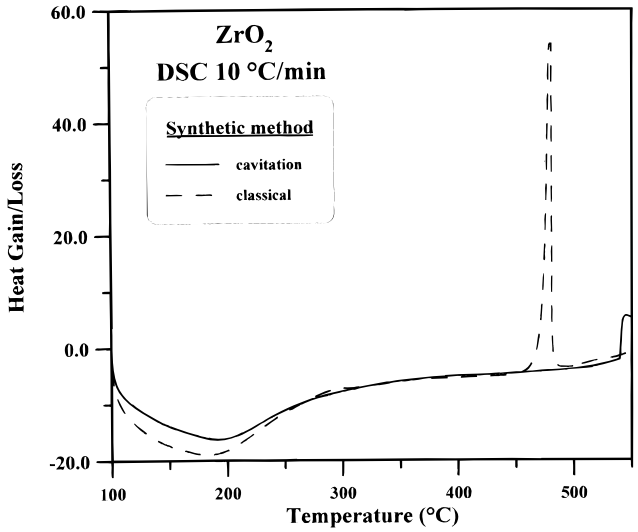


**Figure 6.** Differential scanning calorimetry (DSC) for cavitation (solid line) and classical (broken line) samples of $ZrO_2$.

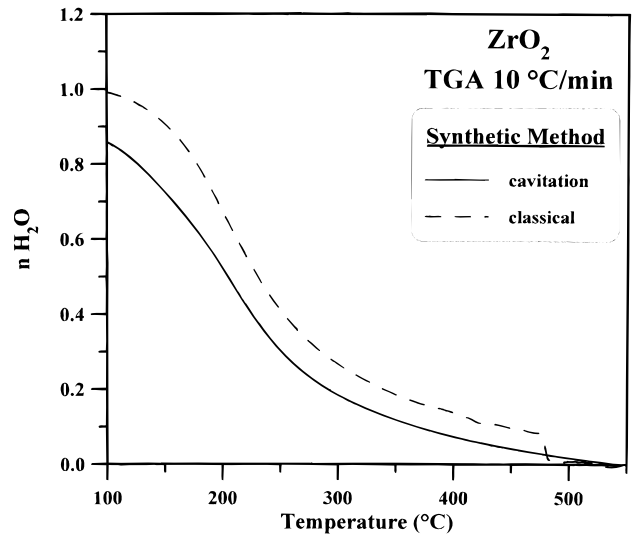


**Figure 7.** Thermal gravimetric analysis (TGA) of cavitation (solid line) and classical (broken line) samples of $ZrO_2$.

$ZrO_2$ prepared in this manner has been previously shown.[21] The dried sample yields no diffraction peaks while the calcined sample shows diffraction peaks corresponding to cubic zirconia. It should be noted that X-ray peak breadths for both the cavitation and classical samples were the same, indicating similar primary particle sizes.

The DSC thermograms for both cavitation (solid) and classical (broken) samples are shown in Figure 6. The sample masses for both experiments were identical. The classical sample shows a sharp exotherm ($T_{cryst}$) at 462 °C, while the cavitation sample shows a somewhat small, broadened exotherm at 530 °C. In both samples, there is an endotherm at low temperature (100−250 °C) which is most likely due to bound water in the samples.

Thermal gravimetric analysis of the cavitation (solid) and classical (broken) samples is shown in Figure 7. The cavitation sample (solid) contains 0.85 $H_2O$/formula and the classical sample contains 1 $H_2O$/formula unit. There is a discontinuity in the water loss at 475 °C for the classical sample. The discontinuity points to a rapid crystallization as opposed to the more gradual crystallization in the cavitation sample.

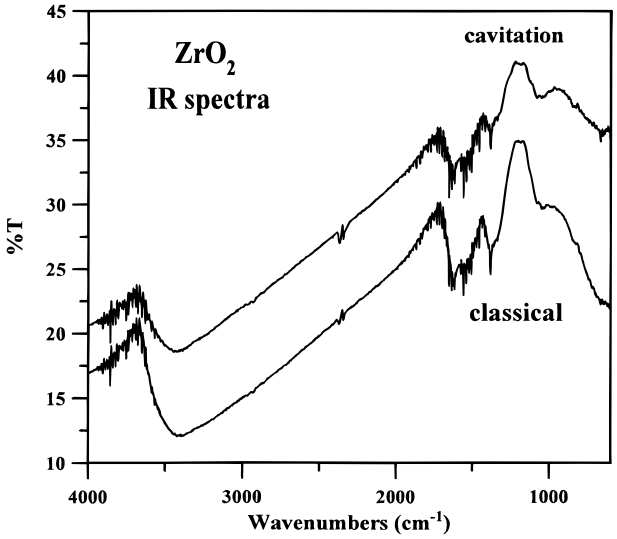


**Figure 8.** Fourier transform infrared spectra (FTIR) for of cavitation (top) and classical (bottom) samples of $ZrO_2$.

Figure 8 shows the IR spectra of the cavitation (top) and classical (bottom) zirconia samples. The samples had identical weight and concentration. The classical spectrum shows a larger absorption in the $OH^-$ stretch region at 3400 $cm^{-1}$. These again are most likely due to more bound surface water in the larger aggregates of the classical sample. A sharper band due to residual $NO_3^-$ at 1340 $cm^{-1}$ is also noted in the classical sample, whereas this band is barely discernable in the material prepared by the cavitation synthesis. This is most likely due to the localized heating that occurs during the cavitation process which causes decomposition of $NO_3^-$ ion.

The infrared and thermal data in this study present an insight to the differences between cavitation and classical processing. The IR spectra in Figure 8 clearly show there is a higher concentration of $NO_3^-$ in the classically prepared sample. Upon calcining at 500 °C, the $NO_3^-$ peak is no longer present in the IR spectra. In addition, the DSC of the classical material (in Figure 6) shows an exotherm which is much larger (higher $\Delta H$) than that in the cavitation sample. The DSC exotherm is coincident with a discontinuous weight loss that does not occur in the cavitation sample. This weight loss and exotherm can be explained by the loss of $NO_3^-$ ion as evidenced by the IR spectra. The cavitation sample has no residual $NO_3^-$ ion due to the decomposition by localized heating during the process.

A previous study on mechanically stressed zirconia hydrogels which exhibit this same behavior offers an alternative explanation.[25] The zirconia hydrogels were pretreated by rotation or vibration milling. A positive shift of 45 °C was noted in the $T_{cryst}$ of the vibration-milled sample in the previous study. The hydrogel study concluded that mechanical stress leads to preordering of the oxygen atoms in the gel. This preordering leads to partial structural stabilization and thus a lower $\Delta H_{cryst}$ (i.e., smaller exotherm). The broadening of the exotherm also indicates a more gradual crystallization. The cavitation synthetic method clearly introduces more mechanical stress during processing. The mechanical stress may be a contributing factor to more rapid crystallization of the $ZrO_2$.

(25) Isobe, T.; Senna, M. *J. Solid State Chem.* **1991**, *93*, 368.

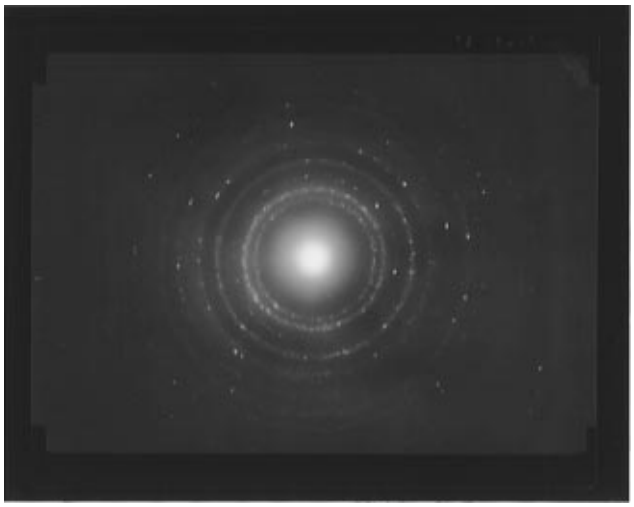

**Figure 9.** Select area diffraction pattern for dried (110 °C) NiO synthesized from $NH_4HCO_3$.

**Table 4. Comparison of SAD *d* Spacings for NiO with JCPDS File for NiO**

| $d_{obsd}$ | $d_{JCPDS}$ | $d_{obsd}$ | $d_{JCPDS}$ |
|---|---|---|---|
| 2.41 | 2.410 | 1.21 | 1.206 |
| 2.09 | 2.088 | 1.04 | 1.0441 |
| 1.48 | 1.476 | 0.96 | 0.9582 |
| 1.26 | 1.259 | 0.94 | 0.9338 |

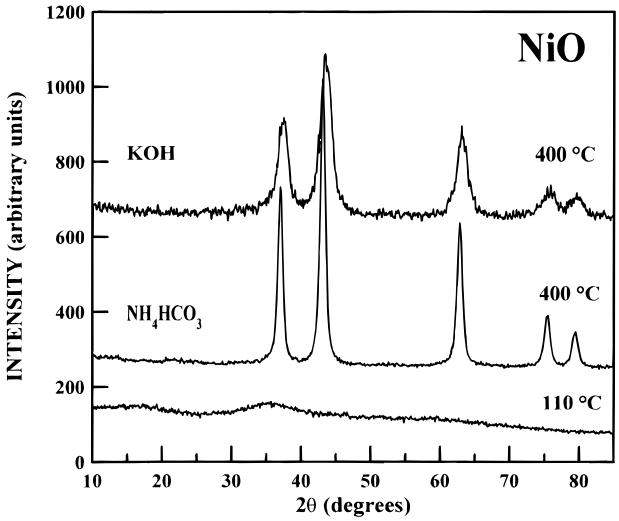


**Figure 10.** X-ray diffraction pattern of NiO prepared from $NH_4HCO_3$ after drying at 110 °C (bottom) and after calcining at 400 °C (middle). X-ray diffraction pattern of KOH-prepared NiO after calcining at 400 °C (top).

**NiO.** Two different precipitating agents ($NH_4HCO_3$ and KOH) were used to complete the NiO synthesis due to the high solubility of the nickel oxide/hydroxide in $NH_4OH$. Both nickel oxide samples were isolated as a green solid upon drying at 110 °C for 12 h.

Select area diffraction of the dried KOH sample yields a pattern of broad rings that can be indexed as $Ni(OH)_2$ with no traces of NiO. Figure 9 shows a SAD pattern of the dried $NH_4HCO_3$ sample that can be indexed as nickel oxide. Table 4 is a comparison of the indexed diffraction rings with the JCPDS entry for nickel oxide. The X-ray diffraction pattern of the dried (110 °C) KOH sample again can be indexed as $Ni(OH)_2$. Figure 10 shows the $NH_4HCO_3$ sample as dried at 110 °C (bottom) and as calcined at 400 °C (middle). The bottom trace in Figure 10 shows no diffraction peaks. The calcined

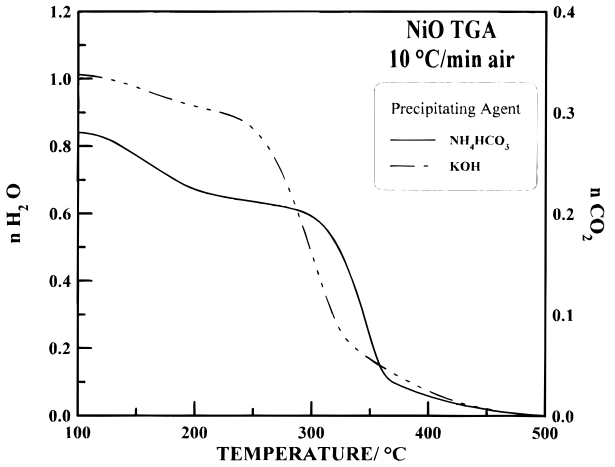


**Figure 11.** Thermal gravimetric analysis (TGA) of NiO prepared from $NH_4HCO_3$ (solid line) and KOH (broken).

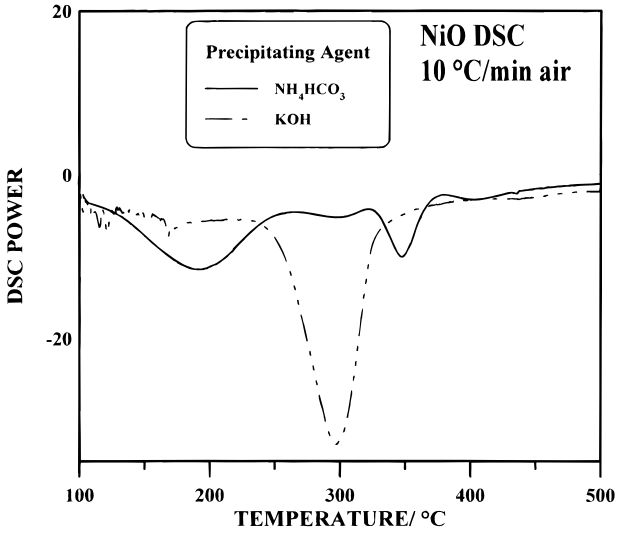


**Figure 12.** Differential scanning calorimetry of NiO prepared from $NH_4HCO_3$ (solid line) and KOH (broken).

sample in the top trace can be indexed as NiO. The particle size of the NiO in Figure 10 is 4.2 nm. It should be noted that upon calcination, however, the KOH sample produces smaller particle NiO. The top trace in Figure 10 is the KOH sample after calcining at 400 °C, which yields a particle size of 2.7 nm.

Figure 11 shows the thermal gravimetric analyses for the $NH_4HCO_3$ (solid) and KOH (broken) samples. The KOH sample has 1 $H_2O$/formula unit, which is consistent with the molecular formula $Ni(OH)_2$. The water loss for the $Ni(OH)_2 \rightarrow NiO$ transition occurs at approximately 300 °C. The $NH_4HCO_3$ sample has 0.2 $H_2O$/formula unit. The water loss at 100−200 °C occurs at a lower temperature than water loss in the $Ni(OH)_2 \rightarrow NiO$ reaction. Therefore, this water is attributed to bound surface water rather than the metal hydroxide. The $NH_4HCO_3$ sample also has 0.2 $CO_2$/formula unit that is lost upon heating to 350 °C. $NiCO_3$ has a 1 $CO_2$/formula unit. In summary, the dried $NH_4HCO_3$ sample has little or no $OH^-$ or $CO_3^-$ ions present. This is consistent with the SAD pattern indicating NiO.

Figure 12 shows the DSC thermograms for the $NH_4HCO_3$ (solid) and KOH (broken) samples. Sample weights for these experiments were identical. The $NH_4HCO_3$ sample (solid) shows endotherms at 200 and 350 °C that correspond to the loss of bound water and $CO_2$, respectively. The KOH sample shows a large endotherm at 300 °C that is attributed to the $Ni(OH)_2 \rightarrow NiO$ reaction. The DSC traces for these compounds clearly show why it is not possible to detect NiO in the dried KOH sample. The $\Delta H_{rxn}$ for $Ni(OH)_2 \rightarrow NiO$ is very large, and thus the equilibrium lies toward the hydroxide. There were attempts to synthesize several other metal oxides (Cu, Zn, Pb) which were unsuccessful due to the formation of the hydroxide over the oxide. Hard−soft ion concepts can be used to explain this. Generally, if the metal ion is soft, it has a greater tendency toward the hydroxide. This can be seen going across the first-row transition metal series. The oxide/hydroxide equilibrium lies toward the oxide until you reach nickel, then it lies toward the hydroxide.

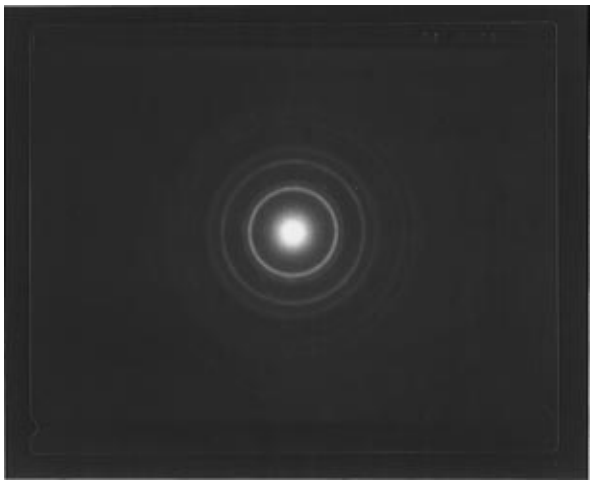

**Figure 13.** Select area diffraction pattern for dried (110 °C) $CeO_2$.

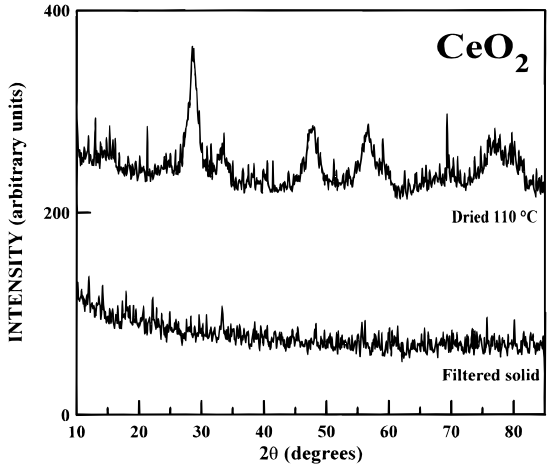


**Figure 14.** X-ray diffraction patterns for the as filtered (bottom) and dried (110 °C) $CeO_2$.

**Table 5. Comparison of SAD *d* Spacings for $CeO_2$ with JCPDS File for $CeO_2$ (Ceria)**

| $d_{obsd}$ | $d_{JCPDS}$ | $d_{obsd}$ | $d_{JCPDS}$ |
|---|---|---|---|
| 3.12 | 3.124 | 1.35 | 1.353 |
| 2.70 | 2.706 | 1.24 | 1.241 |
| 1.91 | 1.913 | 1.21 | 1.210 |
| 1.63 | 1.632 | 1.10 | 1.1044 |
| 1.56 | 1.562 | 1.04 | 1.0412 |

**$CeO_2$.** Ceria was isolated as a yellow solid upon drying at 110 °C for 12 h. Figure 13 shows a SAD pattern that can be indexed as ceria. Table 5 is a comparison of the indexed diffraction rings with the

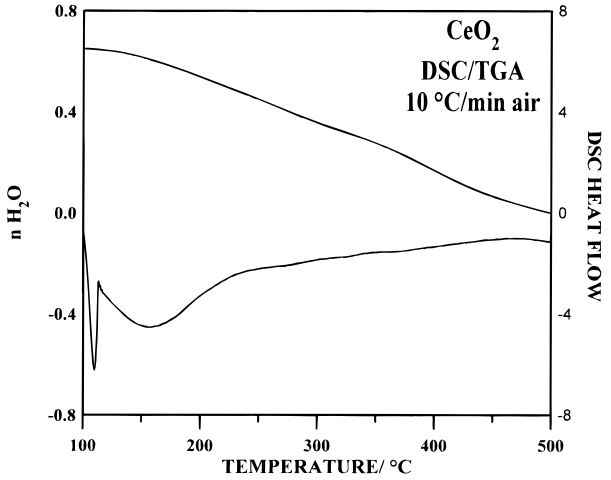


**Figure 15.** Thermal gravimetric analysis (top) and differential scanning calorimetry (bottom) for $CeO_2$.

JCPDS entry for ceria. The X-ray diffraction patterns for the filtered (bottom) and dried at 110 °C (top) are shown in Figure 14. The filtered sample (bottom trace) shows no visible diffraction peaks. The dried sample (top trace) begins to show diffraction peaks that can be indexed as $CeO_2$.

The TGA/DSC of the ceria sample is shown in Figure 15. The nanophase $CeO_2$ has 0.65 $H_2O$/formula unit, while $Ce(OH)_4$ has 2 $H_2O$/formula unit. The DSC trace shows a sharp endotherm at 100 °C followed by a much broader endotherm. This compound is synthesized with Ce(III) nitrate and upon filtering is a purple color that indicates presence of the Ce(III) ion. The dried compound turns to yellow, indicating Ce(IV) ion. The sharp endotherm is attributed to the formation of the $CeO_2$ structure type due to oxidation of the Ce ion. The broad endotherm is the loss of water.

**$Co_3O_4$ and Others.** Cobalt(II,III) oxide was isolated as a dark green solid upon drying at 110 °C for 12 h. Figure 16 shows a SAD pattern that can be indexed as cobalt(II,III) oxide. In addition, it was possible to prepare $Y_2O_3$, $Cr_2O_3$, and $Fe_2O_3$ using the described process. Similar results are attained for these compounds and will not be described in detail. Detailed results for $Fe_2O_3$ have been shown previously.[21]

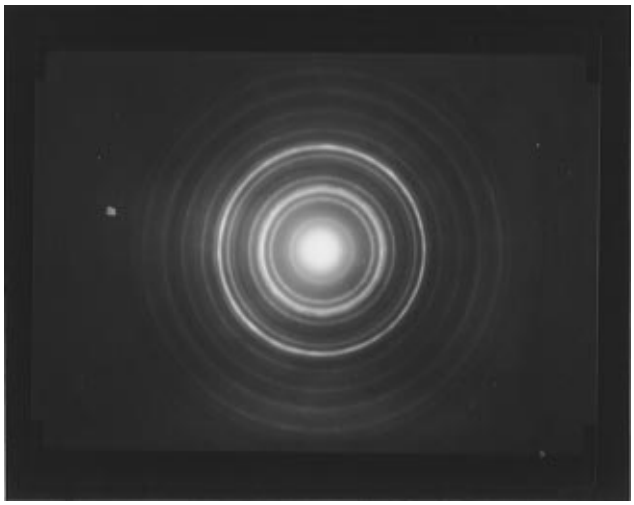

**Figure 16.** Select area diffraction for dried (110 °C) $Co_3O_4$.

## Conclusions

It has been shown by select area diffraction that it is possible to synthesize several nanostructured simple oxides by hydrodynamic cavitation. Select area diffraction shows crystallinity following drying at 110 °C in materials which in most cases have no peaks in the X-ray diffraction pattern. All the diffraction patterns were compared with known hydroxides and oxyhydroxides in the JCPDS file. Comparison of cavitation and classical samples shows that although primary particle sizes are roughly the same, aggregate sizes are markedly decreased. The thermal data indicate that the larger aggregates in the classical samples hold more water and have slower water loss due to diffusion. In addition, this study in conjunction with some previous studies shows that application of mechanical stress causes a change in the amorphous/crystalline equilibrium toward crystallization.

**Acknowledgment.** The authors wish to thank Prof. R. Biedermann and George Schmidt for their help with the transmission electron microscopy. This work was supported by a joint grant from Microfluidics, Inc. of Newton, MA, and Catalytica of Mountain View, CA.

CM950609C